

Constraining the Hubble constant with scattering in host galaxies of fast radio bursts

Tsung-Ching Yang^{1,*}, Tetsuya Hashimoto¹, Tzu-Yin Hsu^{2,3}, Tomotsugu Goto^{2,4}, Chih-Teng Ling⁴, Simon C.-C. Ho^{5,6,7,8}, Amos Y.-A. Chen², and Ece Kilerci⁹

¹ Department of Physics, National Chung Hsing University, 145, Xingda Road, Taichung, 40227, Taiwan (R.O.C.)

² Department of Physics, National Tsing Hua University, 101, Section 2, Kuang-Fu Road, Hsinchu, 30013, Taiwan (R.O.C.)

³ Institute of Astronomy and Astrophysics, Academia Sinica, 11F of AS/NTU Astronomy-Mathematics Building, No.1, Section 4, Roosevelt Road, Taipei 10617, Taiwan (R.O.C.)

⁴ Institute of Astronomy, National Tsing Hua University, 101, Section 2, Kuang-Fu Road, Hsinchu, 30013, Taiwan (R.O.C.)

⁵ Research School of Astronomy and Astrophysics, The Australian National University, Canberra, ACT 2611, Australia

⁶ Centre for Astrophysics and Supercomputing, Swinburne University of Technology, P.O. Box 218, Hawthorn, VIC 3122, Australia

⁷ OzGrav: The Australian Research Council Centre of Excellence for Gravitational Wave Discovery, Hawthorn, VIC 3122, Australia

⁸ ASTRO3D: The Australian Research Council Centre of Excellence for All-sky Astrophysics in 3D, ACT 2611, Australia

⁹ Sabancı University, Faculty of Engineering and Natural Sciences, 34956, Istanbul, Turkey

Received 23 May 2024; accepted 21 October 2024

ABSTRACT

Aims. Measuring the Hubble constant (H_0) is one of the most important missions in astronomy. Nevertheless, recent studies exhibit differences between the employed methods.

Methods. Fast radio bursts (FRBs) are coherent radio transients with large dispersion measures (DM) with a duration of milliseconds. DM_{IGM} , the free electron column density along a line of sight in the intergalactic medium (IGM), could open a new avenue for probing H_0 . However, it has been challenging to separate DM contributions from different components (i.e., the IGM and the host galaxy plasma), and this hampers the accurate measurements of DM_{IGM} and hence H_0 . We adopted a method to overcome this problem by using the temporal scattering of the FRB pulses due to the propagation effect through the host galaxy plasma (scattering time). The scattering-inferred DM in a host galaxy improves the estimate of DM_{IGM} , which in turn leads to a better constraint on H_0 . In previous studies, a certain value or distribution has conventionally been assumed of the dispersion measure in host galaxies (DM_h). We compared this method with ours by generating 100 mock FRBs, and we found that our method reduces the systematic (statistical) error of H_0 by 9.1% (1%) compared to the previous method.

Results. We applied our method to 30 localized FRB sources with both scattering and spectroscopic redshift measurements to constrain H_0 . Our result is $H_0 = 74^{+7.5}_{-7.2} \text{ km s}^{-1} \text{ Mpc}^{-1}$, where the central value prefers the value obtained from local measurements over the cosmic microwave background. We also measured DM_h with a median value of $103^{+68}_{-48} \text{ pc cm}^{-3}$.

Conclusions. The DM_h had to be assumed in previous works to derive DM_{IGM} . Scattering enables us to measure DM_{IGM} without assuming DM_h to constrain H_0 . The reduction in systematic error is comparable to the Hubble tension ($\sim 10\%$). Combined with the fact that more localized FRBs will become available, our result indicates that our method can be used to address the Hubble tension using future FRB samples.

Key words. (Cosmology:) cosmological parameters – (Galaxies:) intergalactic medium – Scattering

1. Introduction

The expansion rate of the Universe is one of the most fundamental physical parameters in astrophysics. The Hubble constant, H_0 , describes the relative expansion rate of the Universe. H_0 has been measured so far with different methods, such as the cosmic microwave background (CMB) (e.g., Planck Collaboration et al. 2020) and local distance ladders (e.g., Riess et al. 2022). How-

ever, there is a difference of 4 to 6σ between the two methods, namely the CMB and the local distance ladder (e.g., Verde et al. 2019; Di Valentino et al. 2021; Riess et al. 2021; Hu & Wang 2023). The recent estimate of H_0 from the CMB by the Planck Collaboration is $67.4 \pm 0.5 \text{ km s}^{-1} \text{ Mpc}^{-1}$ (Planck Collaboration et al. 2020), while the local distance ladder method by the Supernova H_0 for the Equation of State (SH0ES) team yielded $H_0 = 73.0 \pm 1.0 \text{ km s}^{-1} \text{ Mpc}^{-1}$ (Riess et al. 2022). One possible solution to the Hubble tension might be so-called early dark energy,

* pipi4017der@gmail.com

which introduces an additional energy density to the early Universe (e.g., Hill & Baxter 2018), although the difference might be explained by observational systematics (e.g., Mörtzell et al. 2022).

Fast radio bursts (FRBs) are enigmatic coherent radio flashes that occur at cosmological distances ($z \gtrsim 0.05$; e.g., Lorimer et al. 2024; Bailes 2022; Petroff et al. 2019). They are characterized by a brief duration of approximately 1 ms and their exceptional brightness (e.g., Lorimer et al. 2007). The dispersion measure (DM) is a unique observable of FRBs. It represents a free electron density along the line of sight to an FRB. The definition of the DM is $DM \equiv \int n_e ds$, where n_e is the electron number density, and ds is the distance segment along the line of sight. The DM is proportional to the amount of plasma along a line of sight between an FRB source and an observer. Therefore, it can be used as an indicator of the redshift and distance to the FRB (Lorimer et al. 2007). The FRBs are critically important for addressing the issues of missing baryons (e.g., Macquart et al. 2020) and the equation of state of dark energy (e.g., Zhou et al. 2014). This made them a significant focus for further research. We rather focus on the Hubble tension in this particular paper because the existing difference between well-established methods (i.e., $\sim 10\%$ systematics), including the CMB and the local distance ladder, underscores the importance of adding a new independent method to the comparison. The FRB method would be useful if it could achieve an accuracy better than $\sim 10\%$ by mitigating the potential systematics in the method in the sense that it can distinguish between the H_0 values derived from the CMB and local distance ladder methods. Our primary focus is on leveraging the DM of FRBs as a unique distance indicator to derive H_0 .

The observed DM (DM_{obs}) can be separated into three main components. One component is DM_{MW} , which is the DM contributed by Milky Way interstellar medium (ISM) and halo. Another is DM_{h} , which is the DM in a galaxy hosting one FRB source (FRB host galaxy). The other is DM_{IGM} , which is the DM in the intergalactic medium (IGM) between the Milky Way and a host galaxy,

$$DM_{\text{obs}} = DM_{\text{MW}} + DM_{\text{IGM}} + \frac{DM_{\text{h}}}{(1 + z_{\text{spec}})}, \quad (1)$$

where z_{spec} is the spectroscopic redshift of the host galaxy. The DM_{h} is divided by $1 + z_{\text{spec}}$ to convert it into the observer's frame, and the DM is given in units of pc cm^{-3} . The DM_{MW} can be divided into two components, the disk and the halo ($DM_{\text{MW}_{\text{disk}}}$ and $DM_{\text{MW}_{\text{halo}}}$, respectively),

$$DM_{\text{MW}} = DM_{\text{MW}_{\text{disk}}} + DM_{\text{MW}_{\text{halo}}}. \quad (2)$$

According to Eq. 9 in Zhou et al. (2014), the cosmic average of DM_{IGM} is proportional to H_0 . The main focus of Zhou et al. (2014) was to discuss a constraint on the w parameter for the equation of state of dark energy with FRBs. In this work, we implement their formalization (their Eq. 9) in our analysis, combined with scattering, to measure H_0 . Therefore, H_0 can be constrained with DM_{IGM} . To derive DM_{IGM} , DM_{h} has to be subtracted from DM_{obs} . However, in previous works (e.g., Hagstotz et al. 2022; Zhao et al. 2022), a certain distribution of DM_{h} was assumed for all FRB samples to calculate DM_{IGM} (see Sect. 6.2 for details). Therefore, there might be unknown systematic uncertainties in DM_{h} and DM_{IGM} in previous works.

The scattering time (τ) is the pulse-broadening effect of radio pulses, including pulsars and FRBs, due to the propagation through the plasma. The scattering time becomes longer when a

radio pulse propagates in a larger amount of plasma with turbulence, and the scattering tail (Petroff et al. 2019) becomes more significant. The scattering time has a minimal impact on the pulse-broadening effect in the Milky Way and IGM (e.g., Cordes et al. 2022). Therefore, we assumed that scattering only occurs within a host galaxy. The scattering time is a similar quantity as the DM_{h} in the sense that both increase with increasing amount of plasma in a host galaxy. Therefore, the scattering time has information on DM_{h} and is proportional to the square of DM_{h} (Cordes et al. 2022). The DM_{h} can be measured based on the observed scattering. This approach is free of the potential systematics involved in the assumption on DM_{h} , that is, either a fixed value of DM_{h} or a fixed shape of the distribution. This marks a novel application of the scattering time in determining DM_{h} , and it might improve the method employed to measure H_0 . We focus on the capability of this approach using scattering to constrain H_0 , while Cordes et al. (2022) used it to constrain the fraction of baryons in the IGM.

Throughout this paper, we assume the Planck 2018 results implemented in Astropy (Planck Collaboration et al. 2020), that is, a Λ cold dark matter cosmology with $(\Omega_{\text{m}}, \Omega_{\text{b}}) = (0.31, 0.049)$.

2. Method

We provide an overview of the method for constraining H_0 with DM and scattering. We followed the formalization presented in Cordes et al. (2022). Cordes et al. (2022) constrained the fraction of baryons in the intergalactic space with a given H_0 . We instead focus on how accurately H_0 can be constrained under their formalization. The scattering time (τ) was used to measure a probability density function (PDF) of DM_{h} , where the PDF is described as a function of two parameters: DM_{h} and $A_{\tau} \tilde{F} G$. These two parameters are discussed in detail in Sect. 2.1. The integration of the PDF over all possible ranges of the two parameters (Cordes et al. 2022) was computed as a function of the redshift to derive the PDF of redshift. Using the 50th percentile of the PDF of the redshift, we can then determine a modeled redshift (z_{model}) that is derived by using DM and τ . z_{model} can be optimized to the observed redshift (z_{spec}) by changing H_0 . The best-fit z_{model} provides us with the measurement of H_0 .

2.1. Measuring DM_{h}

We adopted this equation to describe the rest-frame τ_{rest} as a function of DM_{h} ,

$$\tau_{\text{rest}}(DM_{\text{h}}, \nu_{\text{rest}}) = C_{\tau} \nu_{\text{rest}}^{-4} A_{\tau} \tilde{F} G \left(\frac{DM_{\text{h}}}{100} \right)^2, \quad (3)$$

where ν_{rest} is the rest-frame frequency in units of GHz. The quantity $C_{\tau} = 0.48 \text{ ms}$ (Cordes et al. 2022) is a numerical constant. To account for how empirical estimates for the scattering time are related to the e^{-1} time, Cordes et al. (2022) introduced a dimensionless factor A_{τ} . $\tilde{F} (\text{pc}^2 \text{ km})^{-1/3}$ is a parameter that characterizes density fluctuations. G is a dimensionless geometric factor. While the three parameters A_{τ} , \tilde{F} , and G have different physical meanings, they appear in the formalization as a product. Therefore, we treated the product $A_{\tau} \tilde{F} G$ as a single parameter. The prior assumption on the $A_{\tau} \tilde{F} G$ range is from 0.001 to 10 $(\text{pc}^2 \text{ km})^{-1/3}$ (Cordes et al. 2022).

Two parameters, DM_h (pc cm^{-3}) and $A_\tau \tilde{F}G$ (ϕ) ($\text{pc}^2 \text{ km}$) $^{-\frac{1}{3}}$, are used to describe the PDF of DM_h (Cordes et al. 2022):

$$f_{DM_h, \phi}(DM_h, \phi | DM_{\text{obs}}, z_{\text{spec}}, \tau_{\text{obs}}) \propto f_{DM_h}(DM_h | DM_{\text{obs}}, z_{\text{spec}}) \times f_\tau(\tau_{\text{obs}} - \hat{\tau}). \quad (4)$$

In Eq. 4, there are two terms on the right side: the first term uses DM , and the second term uses τ . The first term, f_{DM_h} , is expressed as

$$f_{DM_h}(DM_h | DM_{\text{obs}}, DM_{\text{MW}}, z_{\text{spec}}) = \frac{f_{DM_{\text{IGM}}}(DM_{\text{IGM}} | DM_{\text{obs}}, DM_{\text{MW}}, z_{\text{spec}})}{1 + z_{\text{spec}}}. \quad (5)$$

f_{DM_h} is determined using the PDF of DM_{IGM} ($f_{DM_{\text{IGM}}}$), where $DM_{\text{IGM}} = DM_{\text{obs}} - DM_{\text{MW}_{\text{disk}}} - DM_{\text{MW}_{\text{halo}}} - \frac{DM_h}{1+z_{\text{spec}}}$. The uncertainty of DM_{MW} can be accounted for by introducing prior PDFs of $DM_{\text{MW}_{\text{disk}}}$ and $DM_{\text{MW}_{\text{halo}}}$ in Eq. 5. We assumed a flat PDF for $DM_{\text{MW}_{\text{disk}}}$ centered at the mean value derived from the NE2001 (Cordes & Lazio 2002) with $\pm 20\%$ deviations (Cordes et al. 2022). A flat PDF of $DM_{\text{MW}_{\text{halo}}}$ was assumed. It ranged from 25 to 80 pc cm^{-3} (Prochaska & Neeleman 2018; Shull & Danforth 2018; Prochaska & Zheng 2019; Yamasaki & Totani 2020). We used a log-normal distribution to characterize $f_{DM_{\text{IGM}}}$ (Cordes et al. 2022). The log-normal in the form, $N(\mu, \sigma)$, is a function of the following parameters:

$$\mu = \ln(\overline{DM_{\text{IGM}}}) - \frac{\sigma^2}{2}, \quad (6)$$

$$\sigma = \sqrt{\ln\left(1 + \left(\frac{\sigma_{DM_{\text{IGM}}}}{\overline{DM_{\text{IGM}}}}\right)^2\right)}, \quad (7)$$

with the cosmic variance of DM_{IGM} ($\sigma_{DM_{\text{IGM}}}$). $\sigma_{DM_{\text{IGM}}}$ is described as follows:

$$\sigma_{DM_{\text{IGM}}(z_{\text{spec}})} = \sqrt{\overline{DM_{\text{IGM}}}(z_{\text{spec}}) DM_c}, \quad (8)$$

where DM_c is a constant, that is, $DM_c = 50 \text{ pc cm}^{-3}$ (McQuinn 2014), and $\overline{DM_{\text{IGM}}}$ is the cosmic average of DM in the nonuniform intergalactic medium. The $\overline{DM_{\text{IGM}}}$ is described as follows:

$$\overline{DM_{\text{IGM}}} = H_0 \times f_{\text{IGM}} \frac{3\Omega_b c(Y_H + \frac{1}{2}Y_p)}{8\pi G m_p} \int_0^z \frac{1 + z_{\text{spec}}}{\Omega_m(1 + z_{\text{spec}})^3 + 1 - \Omega_m} dz \quad (9)$$

for a flat Λ CDM Universe. The proton mass is $m_p = 1.67 \times 10^{-27}$ kg, and $Y_H = \frac{3}{4}$ and $Y_p = \frac{1}{4}$ are the mass fractions of hydrogen and helium, respectively (Zhou et al. 2014). The fraction of baryons in the IGM is $f_{\text{IGM}} = 0.85 \pm 0.05$ (Cordes et al. 2022). The matter and baryon density are Ω_m and Ω_b (Zhou et al. 2014), respectively. For the cosmological parameters, we used the Planck 2018 results implemented in Astropy (Planck Collaboration et al. 2020).

In the second term of Eq. 4, f_τ is the PDF of $\tau_{\text{obs}} - \hat{\tau}$, where τ_{obs} is the observed scattering, and $\hat{\tau}$ is the theoretical value of the scattering. $\hat{\tau}$ is described as follows:

$$\hat{\tau} = C_\tau \nu_{\text{obs}}^{-4} \phi \left(\frac{DM_h}{100}\right)^2 (1 + z_{\text{spec}})^{-3}, \quad (10)$$

where $C_\tau = 0.48 \text{ ms}$ (Cordes et al. 2022). The observed frequency ν_{obs} is given in units of GHz, and ϕ is the $A_\tau \tilde{F}G$ parameter (Cordes et al. 2022).

A Gaussian function was assumed to express $f_\tau(\tau_{\text{obs}} - \hat{\tau})$ (Fig. 1 top). In the Gaussian function, the mean value was 0, and the observed error in the scattering (σ_τ) was adopted as the standard deviation. However, some FRBs only have upper limits of the scattering. In these cases, we assumed a flat PDF of $\tau_{\text{obs}} - \hat{\tau}$ (Fig. 1 bottom). We adopted $3\sigma_\tau$ as the upper bound of the flat PDF.

To visualize Eq. 4, we show the PDF of DM_h as a function of DM_h and $A_\tau \tilde{F}G$ in the top panels of Fig. 2, where $H_0 = 74.3 \text{ km s}^{-1} \text{ Mpc}^{-1}$ was assumed. By integrating $A_\tau \tilde{F}G$ from 0.001 to 10 ($\text{pc}^2 \text{ km}$) $^{-\frac{1}{3}}$, we present the PDF of DM_h in the bottom panels of Fig. 2.

2.2. Redshift PDF

We used the following equation to calculate the redshift PDF (f_z) with the parameters of DM_{obs} and τ_{obs} :

$$f_z(z | DM_{\text{obs}}, \tau_{\text{obs}}) \propto \iint dDM_h d\phi f_{DM_h, \phi}(DM_h, \phi) \times f_\tau(\tau_{\text{obs}} - \hat{\tau}), \quad (11)$$

where the integration range of DM_h was [20, 1600] pc cm^{-3} (Cordes et al. 2022). In Eq. 11, we calculate the integration of all possible DM_h and $A_\tau \tilde{F}G$, which provided us with f_z .

To demonstrate f_z , we show examples of nine FRBs assuming $H_0 = 74.3 \text{ km s}^{-1} \text{ Mpc}^{-1}$ in Fig. 3. Following Cordes et al. (2022), we present two prior assumptions on the $A_\tau \tilde{F}G$ range in this work: narrow [0.5, 2] and wide [0.001, 10] ($\text{pc}^2 \text{ km}$) $^{-\frac{1}{3}}$. The possible impact on the H_0 measurement with different prior assumptions on the $A_\tau \tilde{F}G$ parameter is discussed in Sects. 3 and 5. Throughout the paper, we present the results assuming the wide range of $A_\tau \tilde{F}G = [0.001, 10]$ ($\text{pc}^2 \text{ km}$) $^{-\frac{1}{3}}$ as a fiducial model unless otherwise mentioned.

2.3. Optimize H_0

We chose the 50 percentile of f_z to define the modeled redshift (z_{model}). By letting H_0 be a parameter (Eq. 9), z_{model} is a function of H_0 . To optimize H_0 , we compared z_{model} and z_{spec} , and we adjusted H_0 so that these two quantities became consistent within their errors, that is, $z_{\text{model}} = z_{\text{spec}}$. In Fig. 4, we show how z_{model} depends on H_0 .

We only changed H_0 in Fig. 4 to demonstrate how this method works using 30 FRB samples (see Sect. 4 and Table 1 for details). However, H_0 degenerates with f_{IGM} in Eq. 9 because the observational error of f_{IGM} is $\sim 6\%$ (e.g., Li et al. 2019; Cordes et al. 2022). Therefore, we present two cases of (i) $f_{\text{IGM}} \times H_0$ as a single parameter in Eq. (9) and (ii) H_0 alone for a given f_{IGM} and its error in Sect. 5.

3. Simulation using mock FRB samples

3.1. Our method using scattering

Before we applied our method to the observed data, we demonstrate how accurate our measurements are compared with a pre-

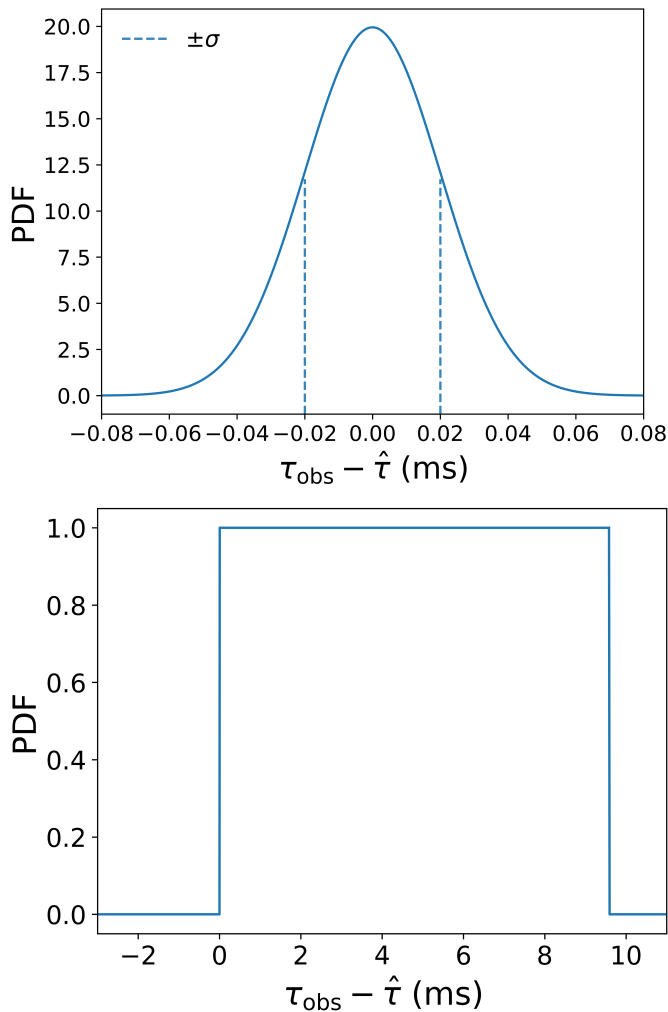


Fig. 1. PDF of $\tau_{\text{obs}} - \hat{\tau}$. Top panel: Case for FRB 20220509G as an example (see Sect. 4 for details), assuming $\log(A_{\tau}\tilde{F}G) = -1$. The peak of the PDF is at $\tau_{\text{obs}} - \hat{\tau} = 0$, and the standard deviation is $\sigma_{\tau} = 0.02$ ms (see also Table 1). Bottom panel: FRBs with an upper limit of the scattering were given a flat PDF. We take FRB 20121102A as an example with the observed scattering of $\tau_{\text{obs}} < 9.6$ ms (Sect. 4 and Table 1), assuming $\log(A_{\tau}\tilde{F}G) = -1$. When $\hat{\tau}$ is lower than 0 or greater than τ_{obs} , the probability is 0. When $\hat{\tau}$ falls between 0 and τ_{obs} , the probability is nonzero and flat. We note that the vertical axes in both panels indicate relative quantities of the probability density.

vious method via simulations. Our aim is a prediction based on a reasonable sample size that can be achieved in the near future. With future instruments such as the CHIME Outrigger (Mena-Parra et al. 2022) and BURSTT (Lin et al. 2022; Ho et al. 2023), it would be feasible to identify 100 FRB host galaxies. Moreover, James et al. (2022) predicted that a sample of approximately 100 FRBs with spectroscopic redshifts would be sufficient to distinguish the $\sim 10\%$ systematic discrepancies of the Hubble tension between the distance ladder and CMB methods. Therefore, we followed James et al. (2022) to decide the sample size of the mock data. We generated 100 mock FRBs as follows. First, we randomly selected redshift values for 100 mock FRBs from the CHIME FRB catalog (CHIME/FRB Collaboration et al. 2021) based on the DM-derived redshift in Hashimoto et al. (2022) to create mock redshifts, z_{mock} . Then, we randomly sampled NE2001 values for 100 FRBs from the same catalog to create mock $DM_{\text{MW,disk}}$ values ($DM_{\text{MW,disk,mock}}$). The adopted value of the

mock $DM_{\text{MW,halo}}$ ($DM_{\text{MW,halo,mock}}$) is 52.5 pc cm^{-3} . Using z_{mock} , we calculated DM_{IGM} based on Eq. (9) assuming $H_0 = 68 \text{ km s}^{-1} \text{ Mpc}^{-1}$ and $f_{\text{IGM}} = 0.85$, where the line-of-sight fluctuation of DM_{IGM} was taken into account based on Eq. (8) to create mock DM_{IGM} values ($DM_{\text{IGM,mock}}$). Figure 5 illustrates the generation of 100 $DM_{\text{IGM,mock}}$.

In general, DM_{h} is highly uncertain because DM_{obs} is an integrated quantity along a line of sight to an FRB, and hence, it is hard to separate between DM_{h} and DM_{IGM} without using scattering. For instance, Macquart et al. (2020) assumed $DM_{\text{h}} = 50 \text{ pc cm}^{-3}$ in their analysis. In contrast, Rafei-Ravandi et al. (2021) conducted a cross-correlation analysis between CHIME FRB samples and galaxy catalogs to conclude that DM_{h} is about 400 pc cm^{-3} , statistically. An even larger average DM_{h} might be suggested by a population-model approach (e.g., Wang & van Leeuwen 2024). These works highlight the significant uncertainty of the typical value of DM_{h} , ranging from $\sim 50 \text{ pc cm}^{-3}$ to $\sim 400 \text{ pc cm}^{-3}$. To generate mock FRBs, we assumed a normal distribution with a mean of 200 pc cm^{-3} and a standard deviation of 50 pc cm^{-3} to create mock DM_{h} values ($DM_{\text{h,mock}}$).

Subsequently, using Eq. (1), we derived 100 mock DM_{obs} values ($DM_{\text{obs,mock}}$) from the z_{mock} , $DM_{\text{IGM,mock}}$, $DM_{\text{MW,mock}}$, and $DM_{\text{h,mock}}$. The mock scattering times (τ_{mock}) at the host frame 1 GHz for the 100 mock FRBs were determined using $DM_{\text{h,mock}}$ with $A_{\tau}\tilde{F}G = 1 \text{ (pc}^2 \text{ km)}^{-\frac{1}{3}}$ and $\nu = 1 \text{ GHz}$ from Eq. 3. τ_{mock} at the observer's frame ($\tau_{\text{mock,obs}}$) was calculated by dividing τ_{mock} by a $(1 + z_{\text{mock}})^3$ factor, assuming ν^{-4} dependence of τ and a time-dilation factor of $(1 + z)$. The mock error in scattering ($\sigma_{\tau_{\text{mock}}}$) was simulated based on the median value of the fractional errors of τ_{obs} in Table (1) (i.e., $\sigma_{\tau_{\text{mock}}} = 5.2\%$). In summary, we generated 100 mock FRBs including z_{mock} , $DM_{\text{IGM,mock}}$, $DM_{\text{MW,mock}}$, $DM_{\text{h,mock}}$, $DM_{\text{obs,mock}}$, $\tau_{\text{mock,obs}}$, and $\sigma_{\tau_{\text{mock}}}$.

Figure 6 displays the PDF of $H_0 \times f_{\text{IGM}}$ and H_0 derived by applying our method to the 100 mock FRBs. The result is $H_0 \times f_{\text{IGM}} = 61.6^{+1.6}_{-2.0} \text{ km s}^{-1} \text{ Mpc}^{-1}$. This value corresponds to $H_0 = 72.5^{+4.7}_{-4.9} \text{ km s}^{-1} \text{ Mpc}^{-1}$, where we assumed $f_{\text{IGM}} = 0.85$ taking the ± 0.05 error of f_{IGM} (Cordes et al. 2022) into account. This reconstructed H_0 is consistent with the assumption made in the simulation, that is, $H_0 = 68.0 \text{ km s}^{-1} \text{ Mpc}^{-1}$ within the statistical error.

3.2. Prior assumptions on the $A_{\tau}\tilde{F}G$ range in our method

In Eq. 11, the prior assumption on the $A_{\tau}\tilde{F}G$ range needs to be specified. Following Cordes et al. (2022), we briefly present how the narrow and wide $A_{\tau}\tilde{F}G$ ranges affect the H_0 measurements based on the 100 FRB mock data. We applied the method described in Sect. 2 to the 100 mock data, assuming $A_{\tau}\tilde{F}G = [0.5, 2]$ and $[0.001, 10] \text{ (pc}^2 \text{ km)}^{-\frac{1}{3}}$. For a given value of $f_{\text{IGM}} = 0.85 \pm 0.05$, the derived H_0 are $70.6^{+4.4}_{-4.8}$ and $72.5^{+4.7}_{-4.9} \text{ km s}^{-1} \text{ Mpc}^{-1}$ for $A_{\tau}\tilde{F}G = [0.5, 2]$ and $[0.001, 10] \text{ (pc}^2 \text{ km)}^{-\frac{1}{3}}$, respectively. These reconstructed H_0 values are consistent with the assumption on $H_0 = 68 \text{ km s}^{-1} \text{ Mpc}^{-1}$ within the errors. This is probably because $A_{\tau}\tilde{F}G = 1 \text{ (pc}^2 \text{ km)}^{-\frac{1}{3}}$ was adopted when the mock FRBs were generated (Sect. 3.1), and the two $A_{\tau}\tilde{F}G$ ranges cover this initial assumption reasonably well. Therefore, in this ideal case, no significant systematics due to the prior $A_{\tau}\tilde{F}G$ assumption are expected. However, this might not be the case when observed data are used to constrain H_0 because the physically reasonable range of $A_{\tau}\tilde{F}G$ is yet to be ascertained (Cordes et al.

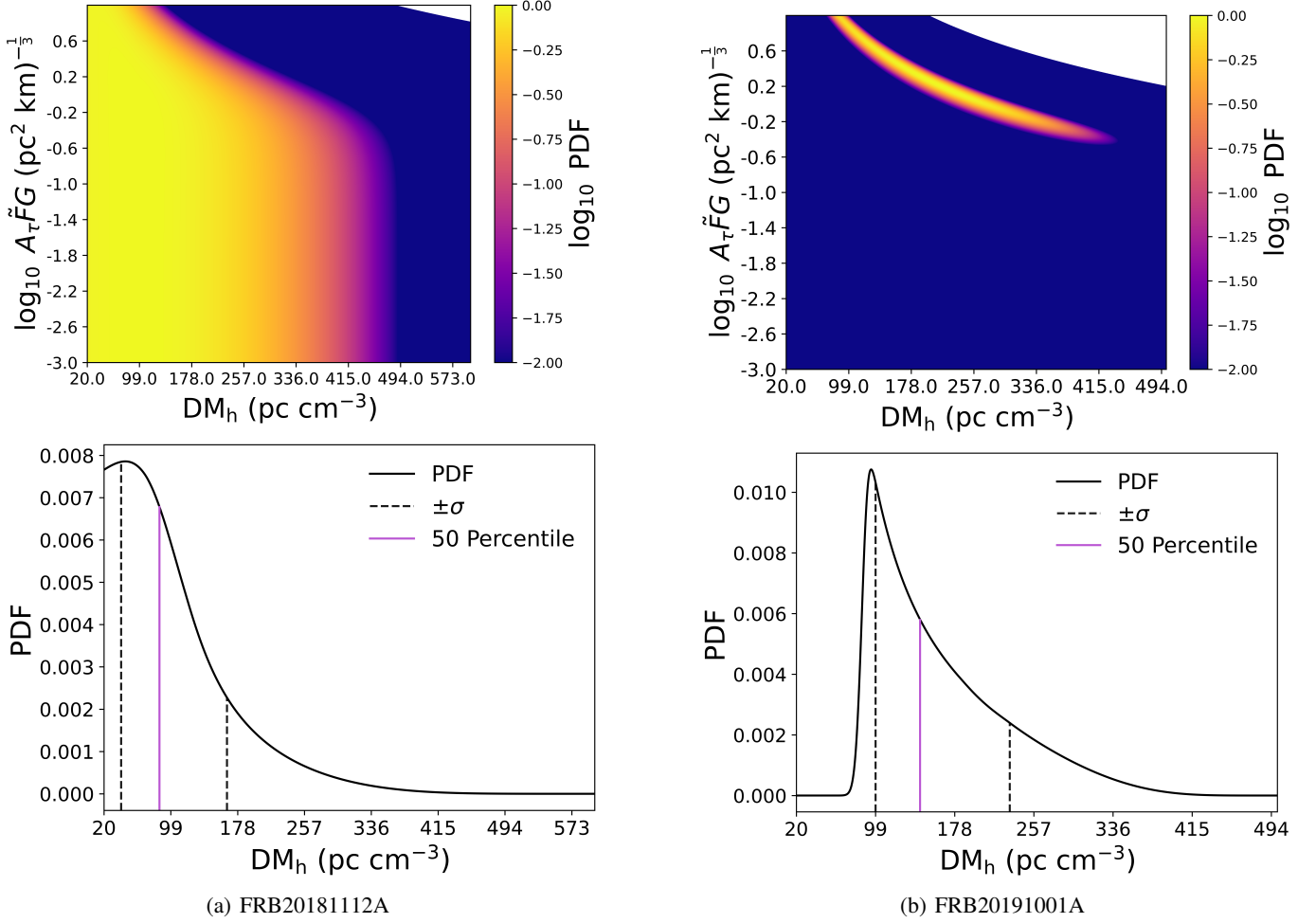


Fig. 2. Two examples of the PDF in our observational samples. Top left panel: Three-dimensional image of f_{DM_h} for FRB 20181112A (see Sect. 4 and Table 1 for details). The x -axis is the DM_h parameter from 20 to 600 pc cm^{-3} . The y -axis is the $A_\tau \tilde{F}G$ parameter from -3 to 1 $(\text{pc}^2 \text{ km})^{-\frac{1}{3}}$ in log scale. For a given DM_h and $A_\tau \tilde{F}G$, the corresponding probability density in the log scale is presented by color. Bottom left panel: Integration of the PDF over the $A_\tau \tilde{F}G$ parameter from 0.001 to 10 $(\text{pc}^2 \text{ km})^{-\frac{1}{3}}$, which provides us with the PDF of DM_h . The purple line shows the 50 percentile of the PDF. The dashed black lines correspond to the 84.2 and 15.8 percentiles of the PDF ($\pm\sigma$). The 50 percentile is $\text{DM}_h = 85.6$ pc cm^{-3} , $+\sigma = 78$ pc cm^{-3} , and $-\sigma = 45.4$ pc cm^{-3} . Top right panel: Example of a 3D image of f_{DM_h} by using FRB 20191001A (see Sect. 4 and Table 1 for details). Bottom right panel: Same as the bottom left panel, but using FRB 20191001A. The 50 percentile is $\text{DM}_h = 143.3$ pc cm^{-3} , $+\sigma = 89.3$ pc cm^{-3} , and $-\sigma = 44.2$ pc cm^{-3} .

2022). A further discussion of using observed data is described in Sect. 6.3.

3.3. Previous FRB method assuming DM_h

For a comparison, we tested a previous method without $\tau_{\text{mock,obs}}$, assuming $\text{DM}_h = 50$ pc cm^{-3} to calculate DM_{IGM} . In this previous method, DM_{IGM} was calculated solely based on Eq. 1 for the same 100 FRB mock samples as were used for our method above. The top panel of Fig. 7 illustrates the resulting DM_{IGM} as a function of z_{mock} . We fit Eq. 9 to the mock data by changing H_0 as a fitting parameter. The derived PDFs of $H_0 \times f_{\text{IGM}}$ and H_0 are shown in the middle and bottom panels of Fig. 7, respectively. The result is $H_0 \times f_{\text{IGM}} = 66.9^{+2.4}_{-2.8}$ $\text{km s}^{-1} \text{ Mpc}^{-1}$. This value corresponds to $H_0 = 78.7^{+5.4}_{-5.7}$ $\text{km s}^{-1} \text{ Mpc}^{-1}$, where we assumed $f_{\text{IGM}} = 0.85$ taking the ± 0.05 error of f_{IGM} into account. This reconstructed H_0 significantly deviates from the assumed value of $H_0 = 68.0$ $\text{km s}^{-1} \text{ Mpc}^{-1}$ in the simulation.

3.4. Comparison between our method and the previous FRB method

Fig. 8 summarizes the systematic difference between the previous method and our method. In Fig. 8, we note that the reconstructed H_0 value with our method is consistent with the assumed value of $H_0 = 68$ $\text{km s}^{-1} \text{ Mpc}^{-1}$ within an uncertainty of 1σ . The 1σ error is presented by the dashed vertical orange lines in Fig. 8, where the assumed value (solid vertical black line) is within this error. Therefore, the reconstructed H_0 with our method does not deviate in a statistically significant way from the assumed value. The apparent offset between our method and the assumed value in Fig. 8 would be due to the statistical fluctuation owing to the random process in generating the mock FRB data. The systematic errors of H_0 are 15.7% and 6.6% for the previous method and our method, respectively. This corresponds to a reduction of the systematic error by 9.1%. By adopting our method, the statistical error slightly decreases from 3.9% to 2.9%, which corresponds to a reduction of 1%. This small reduction is probably due to a systematic effect, where the intrinsic variation in DM_h

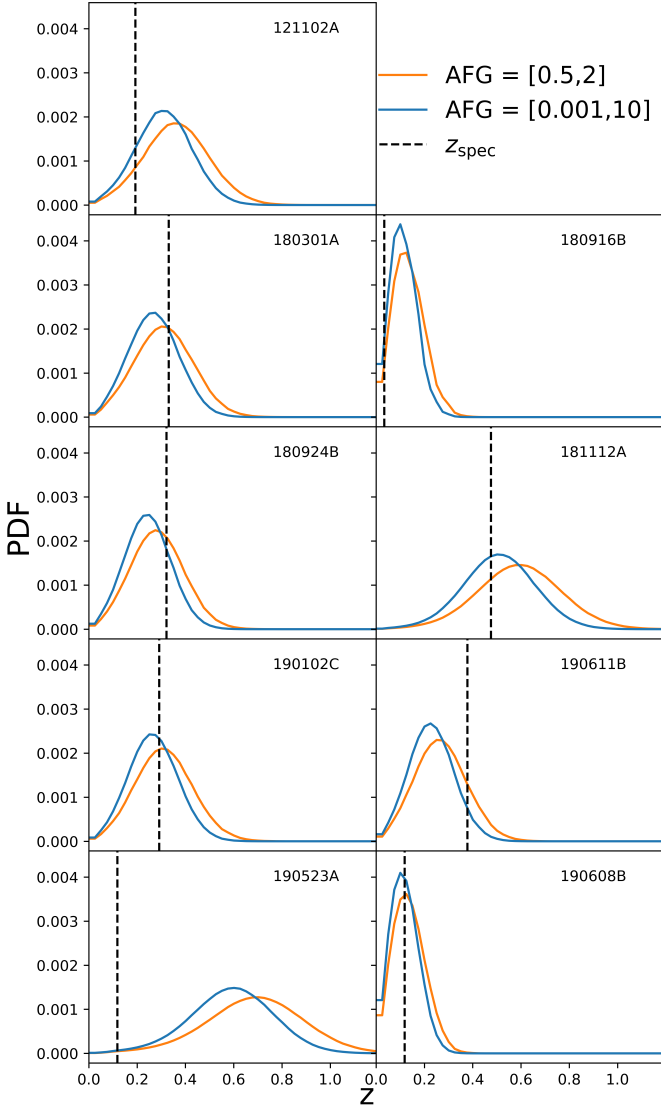


Fig. 3. Nine examples representing the PDFs of redshift (z). These were randomly selected from our FRB samples (see Sect. 4 and Table 1 for details). $H_0 = 74.3 \text{ km s}^{-1} \text{ Mpc}^{-1}$ and $\text{DM}_h = [20, 1600] \text{ pc cm}^{-3}$ were adopted. In each panel, we present PDFs based on two different ranges of $A_\tau \tilde{F}G$: $[0.5, 2]$ (orange line) and $[0.001, 10]$ ($\text{pc}^2 \text{ km}^{-\frac{1}{3}}$). The vertical dashed black line shows the observed redshift (z_{spec}) in each panel.

contaminates the DM_{IGM} variation in the previous method, while our method reduces this contamination by measuring the individual DM_h from scattering. Notably, the reduction in the systematic error is closely aligned with the systematics of the Hubble tension, that is, an $\sim 10\%$ systematic uncertainty. This highlights the potential of our method to address the Hubble tension using forthcoming FRB datasets.

4. Selection criteria for the observed FRB samples

In the previous section, we applied our method to the simulated mock FRB samples to demonstrate how our method works compared with the previous method. In this section, we apply our method as described in Sect. 2 to 30 localized FRBs, which are shown in Table 1. In our method, we require localized FRBs with measurements of the spectroscopic redshift. Although more than

700 FRBs have been detected so far¹, only ~ 40 of them are localized to host galaxies (e.g., Bhandari et al. 2022; Law et al. 2024). Additionally, our method requires information about the scattering time, which meant that we were left with 37 data sets to work with. According to Cordes et al. (2022), the reasonable range of the $A_\tau \tilde{F}G$ parameter is smaller than $10 (\text{pc}^2 \text{ km})^{-\frac{1}{3}}$. The PDF of the $A_\tau \tilde{F}G$ parameter can be computed by integrating Eq. 4 (the top panels of Fig. 2) over DM_h . We found that the PDFs of the $A_\tau \tilde{F}G$ parameter peak beyond $10 (\text{pc}^2 \text{ km})^{-\frac{1}{3}}$ for four FRB samples, that is, FRBs 20191228A, 20210405I, 20210410D, and 20220912A. Their PDFs of the $A_\tau \tilde{F}G$ parameter are mostly distributed at $A_\tau \tilde{F}G > 10 (\text{pc}^2 \text{ km})^{-\frac{1}{3}}$. The range of the peaks is $A_\tau \tilde{F}G = [10, 1000] (\text{pc}^2 \text{ km})^{-\frac{1}{3}}$ for these four samples. Therefore, we excluded these four FRBs from our samples as outliers in the $A_\tau \tilde{F}G$ parameter.

We also excluded three FRB samples that had negative DM_{IGM} as follows. The extragalactic component of the dispersion measure (DM_{EG}) is described as

$$\text{DM}_{\text{EG}} \equiv \text{DM}_{\text{IGM}} + \frac{\text{DM}_h}{1 + z_{\text{spec}}} = \text{DM}_{\text{obs}} - \text{DM}_{\text{MW,disk}} - \text{DM}_{\text{MW,halo}}, \quad (12)$$

where $\text{DM}_{\text{MW,halo}} = 52.5 \text{ pc cm}^{-3}$, and $\text{DM}_{\text{MW,disk}}$ was adopted from the NE2001 model. Here, certain values were used for $\text{DM}_{\text{MW,halo}}$ and $\text{DM}_{\text{MW,disk}}$ for the sample selection alone. The PDFs of $\text{DM}_{\text{MW,halo}}$ and $\text{DM}_{\text{MW,disk}}$ were taken into account in our method (Sect. 2) to constrain H_0 . We found that DM_{EG} of FRB 20200120E and 20220319D are negative, indicating a negative DM_{IGM} . The DM_{EG} of FRB 20181030A is 9.93 pc cm^{-3} . This value is lower than the lower bound of the prior assumption on $\text{DM}_h (= 20 \text{ pc cm}^{-3})$ adopted in this work, following Cordes et al. (2022). These three FRBs correspond to negative DM_{IGM} . Therefore, we also excluded these three FRBs from our analysis. We excluded 7 of the 37 data sets, and the remaining 30 FRB samples were used in this work. Table 3 lists the 7 FRBs we excluded from our samples. In Fig. 9, we compare the scattering time at the rest-frame 1 GHz and DM_{EG} for the 30 FRB samples, along with 5 samples out of 7 excluded samples. We only show 5 excluded samples because 2 of the 7 have a negative DM_{EG} . These 5 excluded samples are close to or above the model line of $A_\tau \tilde{F}G = 10 (\text{pc}^2 \text{ km})^{-\frac{1}{3}}$ (solid green line in Fig. 9). The empirical relation between the scattering at the rest-frame 1 GHz and DM_h expected from Galactic pulsar observations is described as

$$\begin{aligned} \log_{10}(\tau_{\text{MW,psr}}) = & \\ \log_{10}(1.9 \times 10^{-7} \text{ ms } \text{DM}_h^{1.5} \times (1 + 3.55 \times 10^5 \text{ DM}_h^3)) & \quad (13) \\ + \log_{10}(3) \pm 0.76, & \end{aligned}$$

(Cordes et al. 2022), which is shown as the shaded blue region in Fig. 9. The term of $\log_{10}(3)$ represents a scaling factor for taking the spherical wavefront difference between pulsars in the Milky Way and FRBs in host galaxies in the extragalactic Universe into account.

5. Results for the observed FRB samples

As described in Sect. 2.3, we treated $f_{\text{IGM}} \times H_0$ as a single parameter to fit z_{model} to z_{spec} . The top panel of Fig. 10 shows the

¹ <https://blinkverse.alkaidos.cn/>

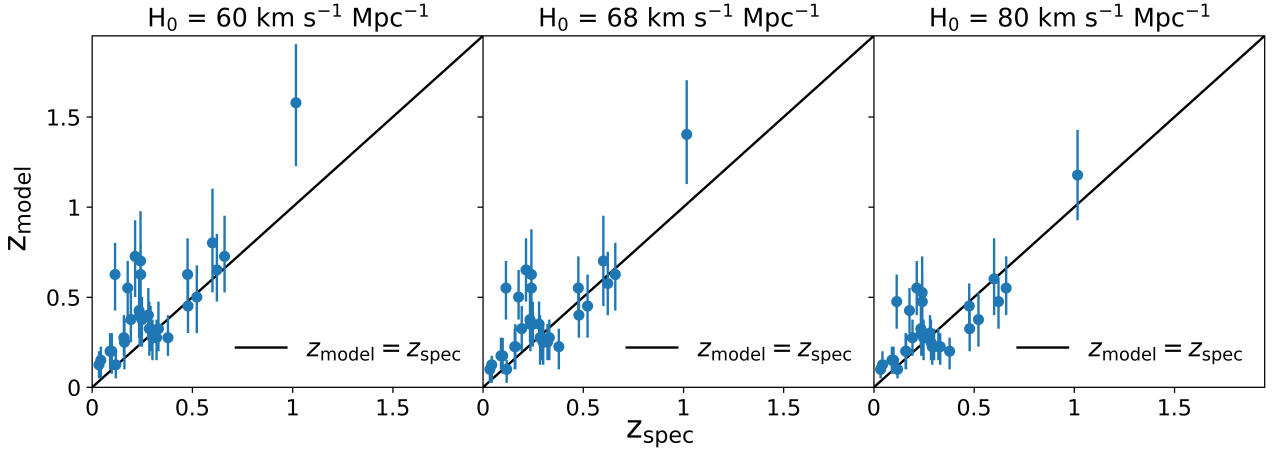


Fig. 4. Observed redshift (z_{spec}) v.s. modeled redshift (z_{model}) to optimize H_0 . To demonstrate how z_{model} depends on H_0 , we present three values of H_0 , 60, 68, and 80 $\text{km s}^{-1} \text{Mpc}^{-1}$, in the different panels. We used 30 FRBs (see Sect. 4 and Table 1 for details) with $\text{DM}_h = [20, 1600] \text{pc cm}^{-3}$ and $A_{\tau\tilde{F}G} = [0.001, 10] (\text{pc}^2 \text{km})^{-\frac{1}{2}}$. The black line corresponds to $z_{\text{model}} = z_{\text{spec}}$.

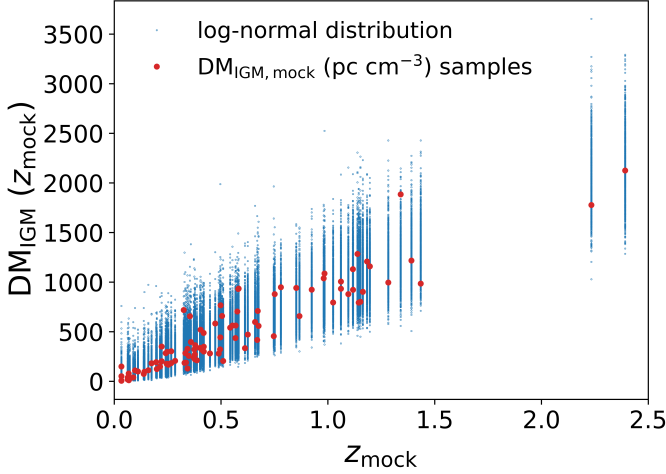


Fig. 5. $\text{DM}_{\text{IGM}, \text{mock}}$ as a function of z_{mock} . The red dots represent $\text{DM}_{\text{IGM}, \text{mock}}$ generated by using Eq. 8 at each z_{mock} , taking the line-of-sight fluctuation of DM_{IGM} into account. For a given z_{mock} , we randomly selected one mock data point (red dot) from the blue dots. We iterated this process 100 times at the different z_{mock} , generating 100 mock FRB data.

χ^2 of the fitting as a function of $f_{\text{IGM}} \times H_0$,

$$\chi^2 = \sum_i \frac{(z_{\text{model},i} - z_{\text{spec},i})^2}{\sigma_i^2}, \quad (14)$$

where σ_i is the error of z_{model} of the i th FRB sample. We calculated the PDF of $f_{\text{IGM}} \times H_0$ assuming $\text{PDF} \propto \exp(-\chi^2/2)$. The result is shown in the middle panel of Fig. 10 with prior assumptions on $\text{DM}_h = [20, 1600] \text{pc cm}^{-3}$, and $A_{\tau\tilde{F}G} = [0.001, 10] (\text{pc}^2 \text{km})^{-\frac{1}{2}}$. The best-fit result is $f_{\text{IGM}} \times H_0 = 63.2^{+4.8}_{-5.2} \text{km s}^{-1} \text{Mpc}^{-1}$. Given $f_{\text{IGM}} = 0.85 \pm 0.05$ (Cordes et al. 2022), the best-fit result corresponds to $H_0 = 74.3^{+7.2}_{-7.5} \text{km s}^{-1} \text{Mpc}^{-1}$, where the uncertainty of f_{IGM} was taken into account (bottom panel of Fig. 10). The median value of DM_h in our analysis is $\text{DM}_h = 103^{+68}_{-48} \text{pc cm}^{-3}$ (see also Table 2 and Fig. 11). These errors were determined by calculating the median of the DM_h errors.

6. Discussion

6.1. Comparison with the CMB and local distance ladders

Our measurement of the Hubble constant is $H_0 = 74.3^{+7.2}_{-7.5} \text{km s}^{-1} \text{Mpc}^{-1}$ using scattering. The central value of this measurement prefers the measurement from the local distance ladder ($H_0 = 73.0 \pm 1.0 \text{km s}^{-1} \text{Mpc}^{-1}$; Riess et al. 2022) than the CMB ($H_0 = 67.7 \pm 0.4 \text{km s}^{-1} \text{Mpc}^{-1}$; Planck Collaboration et al. 2020). However, our measurement is still consistent with these two methods within the 1σ error. To address the Hubble tension with FRBs, both statistical and systematic errors have to be reduced in the future, as discussed in the following sections.

6.2. Comparison with the other FRB methods

Recently, some papers reported H_0 values that were constrained by FRBs, and the methods differed from ours. Hagstotz et al. (2022) assumed a normal distribution of DM_h with $\mu = 100 \text{pc cm}^{-3}$ and $\sigma = 50 \text{pc cm}^{-3}$. They derived $H_0 = 62.3 \pm 9.1 \text{km s}^{-1} \text{Mpc}^{-1}$ using the $\text{DM}_{\text{IGM}}-z$ relation with nine localized FRB samples. They assumed $f_{\text{IGM}} = 0.84$, where the difference from our assumption, $f_{\text{IGM}} = 0.85$, is negligibly small compared to the uncertainty of H_0 . James et al. (2022) combined FRB population models and the $\text{DM}_{\text{EG}}-z$ relation, which were parameterized by seven quantities for fitting, including μ and σ of the lognormal distribution of DM_h and H_0 . They fit the model to the 76 FRB data obtained from The Commensal Real-time The Australian Square Kilometre Array Pathfinder Fast Transients Coherent (CRACO) survey (16 localized and 60 unlocalized), where the best-fit model indicates $H_0 = 73^{+12}_{-8} \text{km s}^{-1} \text{Mpc}^{-1}$, $\mu = 186^{+59}_{-48} \text{pc cm}^{-3}$, and $\sigma = 3.5 \text{pc cm}^{-3}$. They assumed $f_{\text{IGM}} = 0.844$. Zhao et al. (2022) used a Bayesian framework to estimate $H_0 = 80.4^{+24.1}_{-19.4} \text{km s}^{-1} \text{Mpc}^{-1}$ with 12 unlocalized FRB samples with a prior assumption on a lognormal distribution of DM_h with $\mu = 68 \text{pc cm}^{-3}$ and $\sigma = 0.88 \text{pc cm}^{-3}$. The samples were collected from FRBs detected with the Australian Square Kilometre Array Pathfinder (ASKAP). These previous works assumed a certain shape of the DM_h distribution, that is, a lognormal distribution or a normal distribution. Our method is free of this assumption. The scattering is used to derive the individual DM_h and DM_{IGM} in the samples.

Table 1. FRB samples.

FRB	DM _{obs}	DM _{MW_{disk,obs}}	v _{obs}	z _{spec}	τ _{obs}	σ _{τ_{obs}}	References		
	(pc cm ⁻³)	(pc cm ⁻³)	(GHz)		(ms)	(ms)	DM _{obs}	z _{spec}	τ _{obs} , v _{obs}
20121102A	557.4 ^{+2.0} _{-2.0}	188	0.5	0.19273 ± 0.0008	< 9.6		1	20	23
20180301A	536 ⁺⁸ ₋₁₃	152	1.35	0.3304	0.71	0.03	2	2	24
20180916B	349.2 ^{+0.3} _{-0.3}	198	0.35	0.0337	< 1.7		3	2	25
20180924A	361.42 ^{+0.06} _{-0.06}	40.5	1.2	0.3214 ± 0.0002	0.68	0.03	4	5	9
20181112A	589.27 ^{+0.03} _{-0.03}	41.7	1.3	0.47550 ± 0.00015	0.0207	0.00085	5	5	26
20190102C	363.6 ^{+0.3} _{-0.3}	57	1.32	0.2913	0.041	0.0025	6	6	9
20190520B	1204.7 ^{+0.4} _{-0.4}	60.2	1.41	0.241 ± 0.001	10.9	1.5	7	7	27
20190523A	760.8 ^{+0.6} _{-0.6}	37.2	1	0.660 ± 0.002	1.4	0.2	8	8	8
20190608B	340.05 ^{+0.06} _{-0.03}	37.3	1.27	0.11778	3.3	0.2	9	9	9
20190611B	321.4 ^{+0.2} _{-0.2}	57.8	1.3	0.378	0.18	0.02	6	9	9
20190614D	959.2 ⁺⁵ ₋₅	87.8	1.4	0.60 ± 0.17	< 3.3		10	10	10
20190711A	593.1 ^{+0.4} _{-0.4}	56.5	1.3	0.522	< 1.12		6	9	28
20190714A	504 ⁺² ₋₂	38.5	1.27	0.2365	< 2		11	21	11
20191001A	506.92 ^{+0.04} _{-0.04}	44.2	0.824	0.2340 ± 0.0001	3.3	0.02	12	12	12
20200430A	380.1 ^{+0.4} _{-0.4}	27.2	0.865	0.1610	< 15		13	21	13
20201124A	413.52 ^{+0.05} _{-0.05}	140	0.865	0.098 ± 0.002	< 9		14	14	29
20210117A	729.1 ^{+0.36} _{-0.23}	34.4	1.2	0.214 ± 0.001	0.33	0.02	15	21	30
20210320C	384.8 ^{+0.3} _{-0.3}	39.3	0.842	0.280	0.247	0.006	16	16	30
20210603A	500.147 ^{+0.004} _{-0.004}	39.5	0.6	0.1772 ± 0.0001	0.155	0.003	17	17	17
20220207C	262.38 ^{+0.01} _{-0.01}	76.1	1.4	0.043040	0.0146	0.0026	18	18	18
20220307B	499.27 ^{+0.06} _{-0.06}	128	1.4	0.248123	0.1139	0.0059	18	18	18
20220310F	462.24 ^{+0.005} _{-0.005}	46.3	1.4	0.477958	0.02164	0.00022	18	18	18
20220418A	623.25 ^{+0.01} _{-0.01}	36.7	1.4	0.622000	0.0928	0.003	18	18	18
20220506D	396.97 ^{+0.02} _{-0.02}	84.6	1.4	0.30039	0.3427	0.0074	18	18	18
20220509G	269.53 ^{+0.02} _{-0.02}	55.6	1.41	0.089400	0.08	0.02	18	22	22
20220610A	1458.15 ^{+0.25} _{-0.55}	31	1.15	1.016 ± 0.002	0.511	0.012	19	19	19
20220825A	651.24 ^{+0.06} _{-0.06}	78.5	1.4	0.241397	0.0817	0.0033	18	18	18
20220914A	631.28 ^{+0.04} _{-0.04}	54.7	1.4	0.113900	< 0.08		18	22	22
20220920A	314.99 ^{+0.01} _{-0.01}	39.9	1.4	0.158239	0.078	0.15	18	18	18
20221012A	441.08 ^{+0.7} _{-0.7}	54.3	1.4	0.284669	< 1.29		18	18	18

References. (1) Spitler et al. (2014); (2) Bhandari et al. (2022); (3) CHIME/FRB Collaboration et al. (2019); (4) Bannister et al. (2019); (5) Prochaska et al. (2019); (6) Macquart et al. (2020); (7) Niu et al. (2022); (8) Ravi et al. (2019); (9) Day et al. (2020); (10) Law et al. (2020); (11) Bhandari et al. (2019); (12) Bhandari et al. (2020); (13) Kumar et al. (2020); (14) Ravi et al. (2022); (15) Bhandari et al. (2023); (16) Shannon (2023); (17) Cassanelli et al. (2023); (18) Law et al. (2024); (19) Ryder et al. (2023); (20) Tendulkar et al. (2017); (21) Simha et al. (2023); (22) Connor et al. (2023); (23) Josephy et al. (2019); (24) Price et al. (2019); (25) Chawla et al. (2020); (26) Cho et al. (2020); (27) Lee et al. (2023); (28) Qiu et al. (2020); (29) Kumar et al. (2021); (30) Sammons et al. (2023).

Our result is $H_0 = 74.3^{+7.2}_{-7.5}$ km s⁻¹ Mpc⁻¹ (Sect. 5), which is consistent with H_0 in these previous works within the statistical errors. In the previous method, however, there might be significant unknown systematics in the assumption on DM_h as we demonstrated in Sect. 3. Depending on the different assumptions on DM_h , the central values of derived H_0 systematically differ

in the previous works mentioned above. This possible systematics is still smaller than the large statistical error based on the current FRB samples. However, the possible systematics would be problematic in the future when the statistical uncertainty is significantly reduced by large FRB samples. In contrast to previous studies, our method can minimize these systematics using

Table 2. DM_h and z_{model} computed for the FRB samples.

FRB	DM_h ($H_0 = 73$) pc cm ⁻³	z_{model}	FRB	DM_h ($H_0 = 73$) pc cm ⁻³	z_{model}
20121102A	58 ⁺²⁵ ₋₆₀	0.301 ± 0.13	20201124A	114 ⁺⁴⁸ ₋₅₄	0.15 ± 0.1
20180301A	141 ⁺⁷² ₋₅₆	0.251 ± 0.1	20210117A	118 ⁺¹¹² ₋₆₄	0.602 ± 0.15
20180916B	33 ⁺¹⁰ ₋₂₃	0.1 ± 0.05	20210320C	48 ⁺⁴⁴ ₋₁₉	0.326 ± 0.1
20180924A	97.5 ⁺⁵⁹ ₋₄₃	0.226 ± 0.1	20210603A	37.1 ⁺⁴⁶ ₋₁₃	0.451 ± 0.13
20181112A	85.6 ⁺⁸⁰ ₋₄₅	0.501 ± 0.15	20220207C	64.1 ⁺³¹ ₋₂₉	0.125 ± 0.075
20190102C	75.2 ⁺⁵² ₋₃₇	0.251 ± 0.1	20220307B	91.4 ⁺⁶⁵ ₋₄₇	0.301 ± 0.13
20190520B	827 ⁺¹⁹⁹ ₋₁₆₁	0.576 ± 0.18	20220310F	89.1 ⁺⁷⁰ ₋₄₇	0.351 ± 0.13
20190523A	178 ⁺¹³³ ₋₅₇	0.576 ± 0.18	20220418A	104 ⁺⁹¹ ₋₅₇	0.526 ± 0.15
20190608B	199 ⁺³³ ₋₃₂	0.1 ± 0.085	20220506D	56.9 ⁺⁵⁶ ₋₄₉	0.226 ± 0.1
20190611B	74.4 ⁺⁴⁶ ₋₃₆	0.226 ± 0.1	20220509G	71.7 ⁺³⁷ ₋₃₃	0.15 ± 0.075
20190614D	297 ⁺¹⁷⁷ ₋₁₆₈	0.652 ± 0.2	20220610A	283 ⁺²⁴⁰ ₋₁₀₁	1.28 ± 0.25
20190711A	133 ⁺¹⁰³ ₋₇₂	0.401 ± 0.15	20220825A	104 ⁺⁹² ₋₅₇	0.501 ± 0.15
20190714A	148 ⁺⁹⁰ ₋₇₉	0.326 ± 0.15	20220914A	56.3 ⁺⁷⁴ ₋₂₅	0.501 ± 0.15
20191001A	143 ⁺⁸⁹ ₋₄₄	0.326 ± 0.13	20220920A	75.9 ⁺⁴⁷ ₋₃₇	0.226 ± 0.075
20200430A	154 ⁺⁶⁴ ₋₇₅	0.201 ± 0.13	20221012A	134 ⁺⁷⁵ ₋₆₉	0.251 ± 0.13

Table 3. FRB samples that we excluded from our analysis either because of (i) outliers in the $A_\tau \tilde{F}G$ parameter space or because (ii) the DM_{EG} is negative.

FRB	DM_{obs} pc cm ⁻³	$DM_{\text{MW,disk,obs}}$ pc cm ⁻³	ν_{obs} GHz	z_{spec}	τ_{obs} ms	$\sigma_{\tau_{\text{obs}}}$ ms	$\tau(1 \text{ GHz})$ ms	DM_{EG} pc cm ⁻³	References DM, z_{spec} , τ_{obs} , ν_{obs}
20191228A	298	33	1.27	0.2432	6.1	0.6	15.9	212	1
20210405I	565	396	1.28	0.066	9.7	0.2	26.4	116	2
20210410D	579	56.2	1.28	0.1415	29.4	2	79.9	470	3
20220912A	228	125	1.41	0.0771	2.63	0.35	10.3	50.3	4
20181030A	104	41.1	0.704	0.0039	< 0.88		0.22	9.93	5
20200120E	87.8	41	1.4	0.0008	< 0.00003		0.00011	-5.63	6
20220319D	111	140	1.4	0.01123	< 0.1		0.38	-81.3	7

References. (1) Bhandari et al. (2022); (2) Driessen et al. (2024); (3) Caleb et al. (2023); (4) Ravi et al. (2023b); (5) CHIME/FRB Collaboration et al. (2021); (6) Nimmo et al. (2022); (7) Ravi et al. (2023a).

the scattering time to derive the individual DM_h rather than assuming a certain DM_h distribution.

6.3. Prior assumption on the $A_\tau \tilde{F}G$ parameter range

Our simulation described in Sect. 3.2 suggests that the prior assumption on the $A_\tau \tilde{F}G$ range does not significantly impact the best-fit result of H_0 , as far as the prior covers the true $A_\tau \tilde{F}G$ value. However, this might not be the case when observed data are used because the true $A_\tau \tilde{F}G$ distribution is unknown (Cordes et al. 2022).

We compared results based on the observed data, assuming narrow and wide ranges of $A_\tau \tilde{F}G = [0.5, 2]$ and $[0.001, 10]$ ($\text{pc}^2 \text{ km})^{-\frac{1}{3}}$, respectively. Figure 12 shows a comparison between the narrow and wide ranges of $A_\tau \tilde{F}G$ in z_{model} versus z_{spec} . The figure includes our 30 FRB samples, where we fixed the value of $f_{\text{IGM}} \times H_0 = 63.2 \text{ km s}^{-1} \text{ Mpc}^{-1}$ to highlight the dif-

ference between the $A_\tau \tilde{F}G$ ranges. χ^2 is 75.1 for the narrow range, and 37.9 is for the wide range. We found that z_{model} with $A_\tau \tilde{F}G = [0.5, 2]$ ($\text{pc}^2 \text{ km})^{-\frac{1}{3}}$ are systematically lower than that with $A_\tau \tilde{F}G = [0.001, 10]$ ($\text{pc}^2 \text{ km})^{-\frac{1}{3}}$, indicating that the different prior assumptions on $A_\tau \tilde{F}G$ systematically affect the H_0 measurement. To demonstrate this point, we present the best-fit z_{model} to z_{spec} for two cases of the $A_\tau \tilde{F}G$ ranges by optimizing $f_{\text{IGM}} \times H_0$ in the top panel of Fig. 13. The best-fit $f_{\text{IGM}} \times H_0$ (and χ^2) are $51.5^{+4.4}_{-4.4} \text{ km s}^{-1} \text{ Mpc}^{-1}$ (58) and $63.2^{+4.8}_{-5.2} \text{ km s}^{-1} \text{ Mpc}^{-1}$ (37.9) for the narrow and wide ranges, respectively (middle panel of Fig. 13). Given a fixed value of $f_{\text{IGM}} = 0.85 \pm 0.05$, these correspond to $H_0 = 60.6^{+6.3}_{-6.3} \text{ km s}^{-1} \text{ Mpc}^{-1}$ and $H_0 = 74.3^{+7.2}_{-7.5} \text{ km s}^{-1} \text{ Mpc}^{-1}$ for the narrow and wide $A_\tau \tilde{F}G$ ranges, respectively (bottom panel of Fig. 13)

The χ^2 value is higher for the narrow $A_\tau \tilde{F}G$ range, suggesting a worse fit to the observed data with $A_\tau \tilde{F}G = [0.5, 2]$ ($\text{pc}^2 \text{ km})^{-\frac{1}{3}}$. This might suggest that the narrow range does not

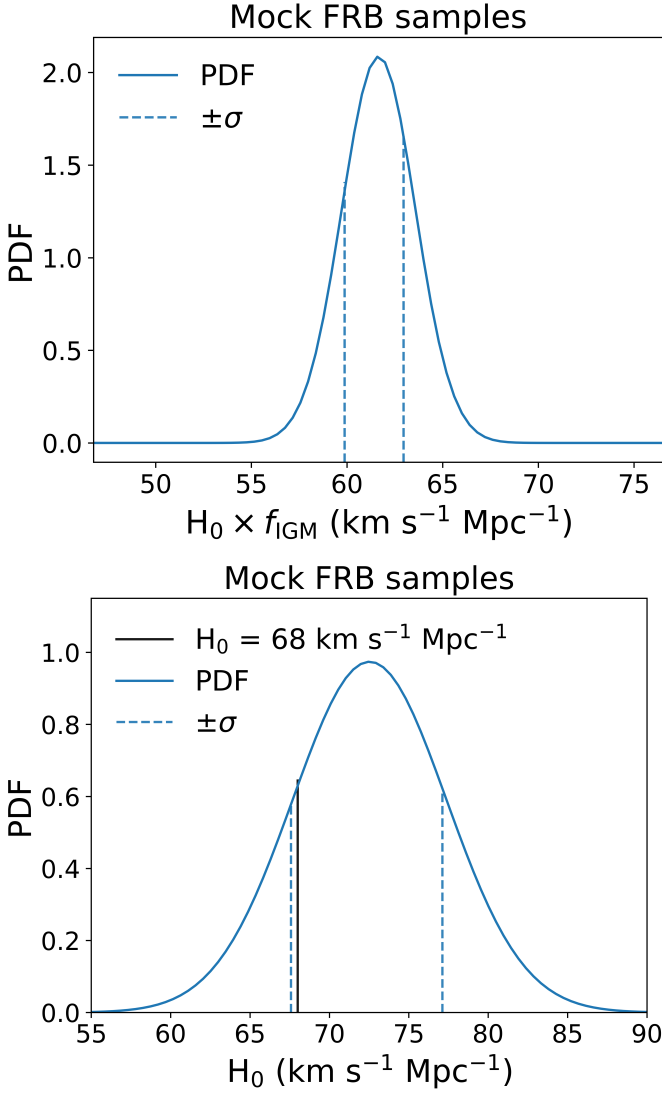


Fig. 6. Simulations of our method with mock FRB samples. Top panel: PDF of $H_0 \times f_{\text{IGM}}$ derived by using the 100 mock FRBs and our method with scattering (blue curve). The vertical dashed blue lines correspond to 84.2 and 15.8 percentiles ($\pm\sigma$) of the PDF. Bottom panel: PDF of H_0 by changing the scale from $H_0 \times f_{\text{IGM}}$ (top panel) to H_0 . To generate the mock data, we assumed $H_0 = 68.0 \text{ km s}^{-1} \text{ Mpc}^{-1}$, which is shown by the solid vertical black line. The vertical dashed blue lines are the positive and negative standard deviations of H_0 after taking the f_{IGM} error into account, where the f_{IGM} error is ± 0.05 (Cordes et al. 2022).

fully cover the true $A_\tau \tilde{F}G$ distribution in the FRB samples. The narrow-range model therefore does not fit the observed data well. In contrast, the wide $A_\tau \tilde{F}G$ range is expected to perform better because its coverage in the $A_\tau \tilde{F}G$ parameter space is better. We speculate that the wide $A_\tau \tilde{F}G$ range covers the true $A_\tau \tilde{F}G$ distribution better, and it would be closer to the ideal situation of our simulation without significant systematics (Sect. 3.2) than the narrow $A_\tau \tilde{F}G$ range. In this sense, the wide $A_\tau \tilde{F}G$ range would be preferable in our analysis.

Detailed investigations of the $A_\tau \tilde{F}G$ impact on $f_{\text{IGM}} \times H_0$ have to be made and the optimal range of $A_\tau \tilde{F}G$ must be determined before our method can address the Hubble tension properly. Physically motivated constraints of the $A_\tau \tilde{F}G$ parameter would also play an important role in searching for the optimal $A_\tau \tilde{F}G$ range. We leave these points as future work because we focused

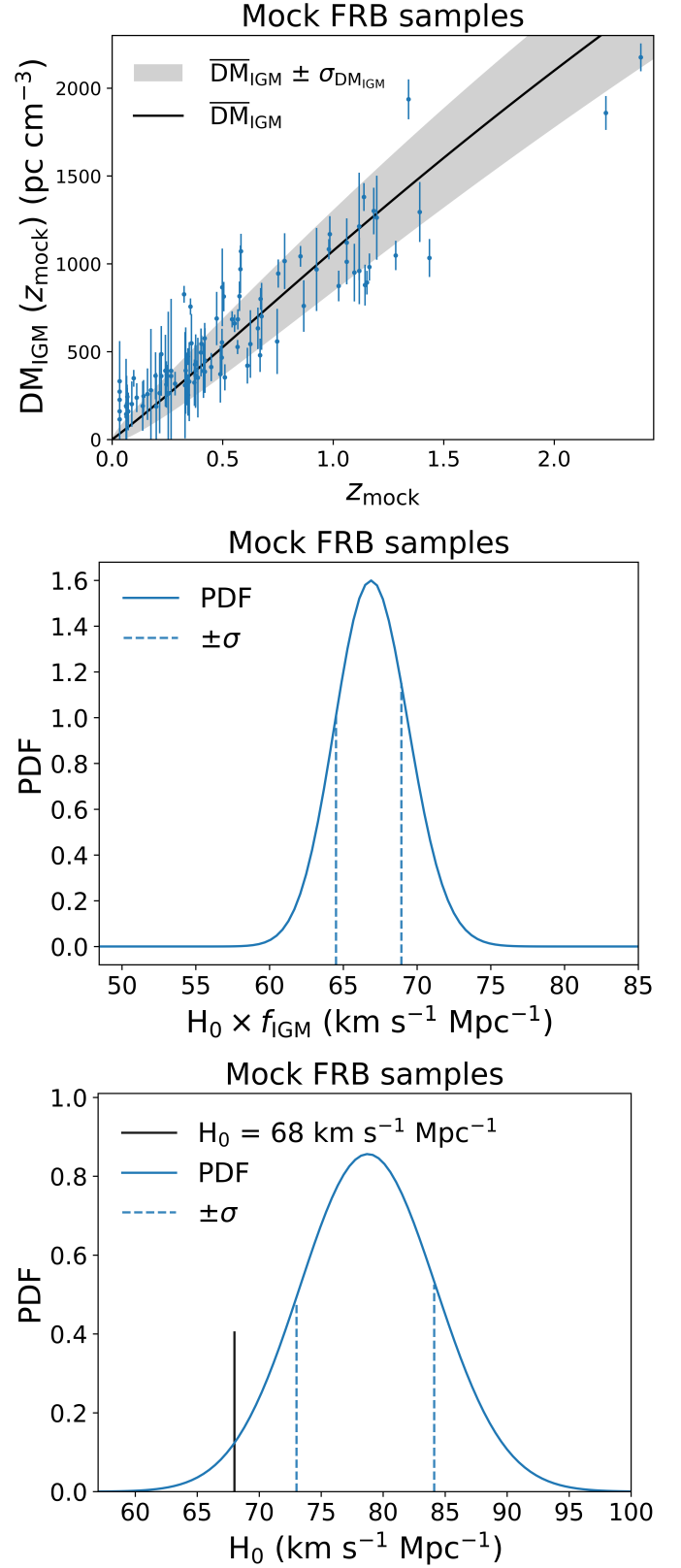


Fig. 7. Simulations of the previous method with mock FRB samples. Top panel: $\text{DM}_{\text{IGM, mock}}$ as a function of z_{mock} . The blue dots with error bars show 100 mock FRB data, where $\text{DM}_{\text{IGM, mock}}$ is calculated by the previous method, assuming $\text{DM}_{\text{h}} = 50 \text{ pc cm}^{-3}$. We fit Eq. 9 to the mock FRB data with a free parameter of H_0 . The best-fit function is shown by the solid black line, where $H_0 = 78.7^{+5.4}_{-5.7} \text{ km s}^{-1} \text{ Mpc}^{-1}$. The gray shaded region indicates the line-of-sight fluctuation of DM_{IGM} described by Eq. 8. Middle panel: Same as the top panel of Fig. 6, but using the previous method, assuming $\text{DM}_{\text{h}} = 50 \text{ pc cm}^{-3}$. Bottom panel: Same as the bottom panel of Fig. 6, but using the previous method, assuming $\text{DM}_{\text{h}} = 50 \text{ pc cm}^{-3}$.

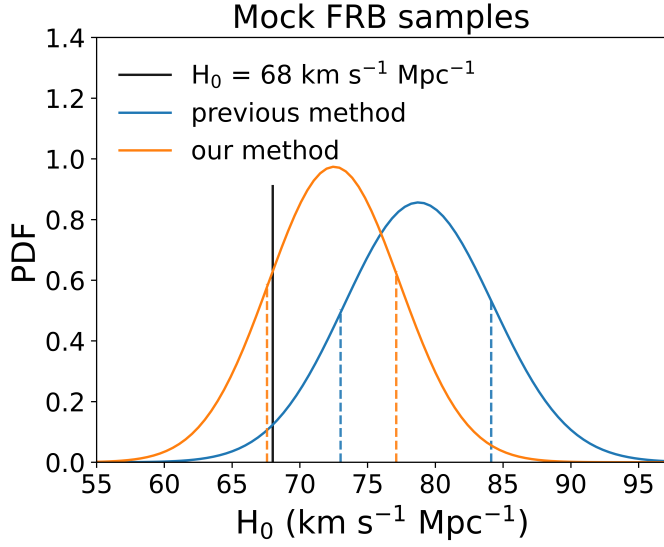


Fig. 8. PDFs of H_0 derived by our method (orange) with positive and negative standard deviations (orange vertical dashed lines) and the previous method (blue) with positive and negative standard deviations (vertical dashed blue lines), using the same 100 mock FRB data. The vertical black line indicates $H_0 = 68.0 \text{ km s}^{-1} \text{ Mpc}^{-1}$, which was assumed when we generated the 100 mock FRBs.

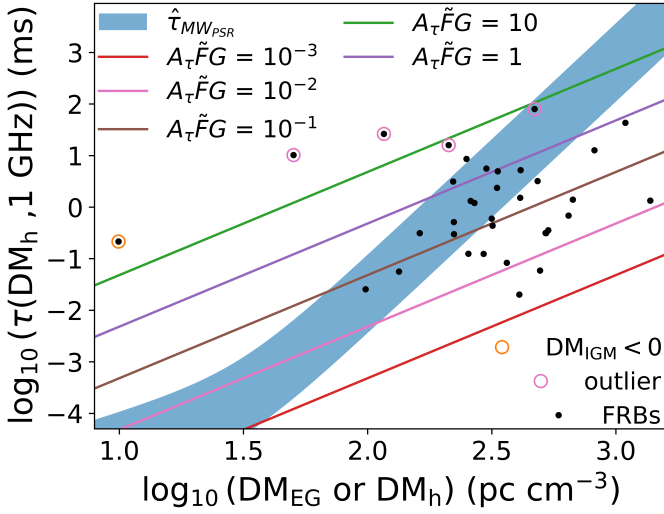


Fig. 9. Scattering time vs. DM_{EG} or DM_h . The x -axis is the DM_{EG} from Eq. (12) in the log scale for the FRB samples (black dots), and it shows DM_h for the empirical relation based on Galactic pulsars (shaded blue region) and the $A_\tau \tilde{F}G$ models (solid colored lines). The y -axis is the scattering time at the rest-frame frequency of 1 GHz in the log scale. The black points are the 30 FRBs in our work. The pink circles are the $A_\tau \tilde{F}G$ outliers in our FRB samples. The orange circle is one of our FRB samples, which is $DM_{IGM} < 0 \text{ pc cm}^{-3}$. The colored lines are the $A_\tau \tilde{F}G$ models from Eq. (3) with $DM_h = [20, 1600] \text{ pc cm}^{-3}$. The blue area is the empirical relation derived from Galactic pulsars described in Eq. (13), which includes the geometrical scaling factor for the FRB samples.

on proposing a method for constraining H_0 with the scattering rather than emphasizing the current accuracy in this paper.

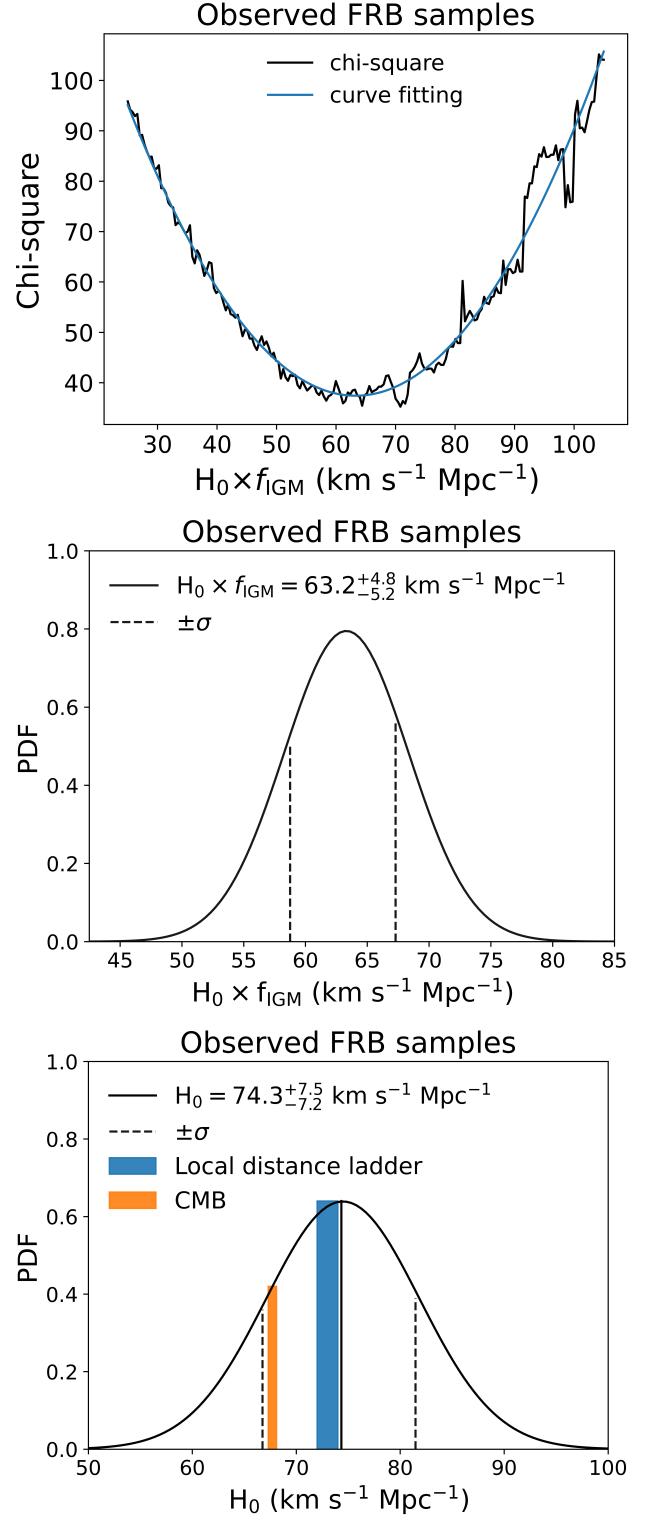


Fig. 10. The results of our method on observed FRB samples. Top panel: χ^2 described by Eq. 14 as a function of $f_{IGM} \times H_0$ using the 30 FRB samples and our method. The black line indicates the χ^2 values derived by changing $f_{IGM} \times H_0$. The blue line is the best-fit polynomial function to χ^2 . Middle panel: PDF of $f_{IGM} \times H_0$ from the χ^2 (top panel). The vertical dashed black lines correspond to the 84.2 and 15.8 percentiles ($\pm\sigma$) of the PDF. Bottom panel: PDF of H_0 by changing the scale from $H_0 \times f_{IGM}$ (middle panel) to H_0 for a given $f_{IGM} = 0.85 \pm 0.05$. The solid vertical line indicates the peak of the PDF, and the dashed vertical lines indicate the uncertainty range of H_0 after taking the 0.05 error of f_{IGM} into account. The orange area indicates the CMB measurement of H_0 (e.g., Planck Collaboration et al. 2020). The blue area shows the measurement by local distance ladders (e.g., Riess et al. 2022).

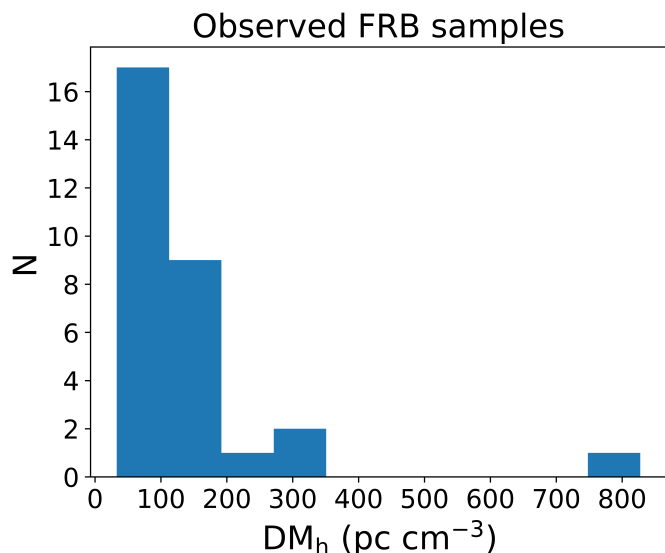


Fig. 11. Histogram of DM_h derived by using scattering (see also Table 2).

6.4. Future FRB samples

Currently, the number of localized FRBs is limited to ~ 40 (e.g., Bhandari et al. 2022; Law et al. 2024). About 100 localized FRBs would be sufficient to clarify the Hubble tension with an uncertainty of $\sim 2.5 \text{ km s}^{-1} \text{ Mpc}^{-1}$ (James et al. 2022). More FRBs will be localized with scattering measurements with future instruments, including the CHIME outrigger (Mena-Parra et al. 2022), the Deep Synoptic Array-110, ASKAP, and the Bustling Universe Radio Survey Telescope in Taiwan (BURSTT) (Lin et al. 2022; Ho et al. 2023). BURSTT can localize ~ 100 FRBs per year (Lin et al. 2022) to identify host galaxies with scattering measurements. Unlocalized FRBs can be used to derive the redshift statistically to further increase the samples (e.g. Zhao et al. 2022). Therefore, our method can be tested with better statistics in the near future.

7. Conclusions

A significant difference of 4 to 6 sigma exists in determining the Hubble constant (H_0) for two distinct methods, the cosmic microwave background (CMB) and the local distance ladders. This difference is most likely caused by unknown systematic errors. Therefore, devising an independent method for measuring H_0 is the most important mission for addressing this unresolved puzzle. The FRBs offer a unique observable, DM_{IGM} , which is a new distance indicator to derive H_0 . We summarize the result of this work below.

1. DM_h had to be assumed in previous works to derive DM_{IGM} . The scattering enabled us to measure DM_{IGM} with a parameter that combined a pulse profile, density fluctuations, and the geometry of a scattering screen ($A_r \tilde{F}G$ parameter). We used this parameterization for 30 FRBs with scattering measurements to model the redshifts, and we compared them with the observed redshifts (spectroscopic redshifts) to constrain H_0 .
2. We demonstrated that our method reduces the systematic error of H_0 by 9.1% compared to the previous method, and the statistical error is reduced by 1%. The reduction in systematic error is comparable to the Hubble tension ($\sim 10\%$),

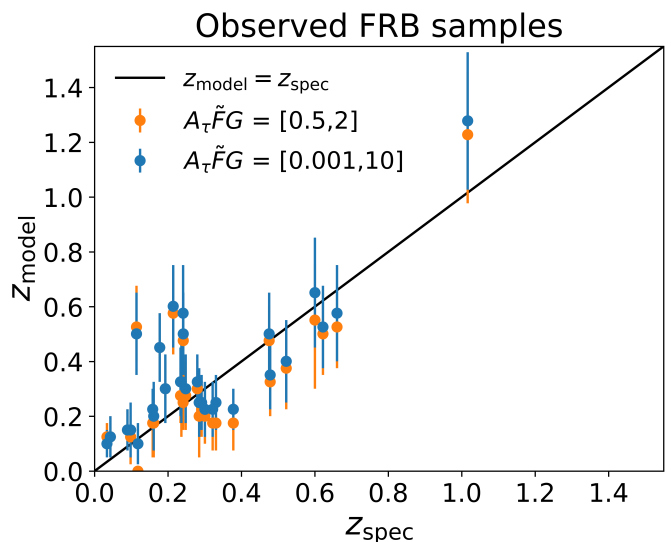


Fig. 12. z_{model} vs. z_{obs} , comparing two prior assumptions on the $A_r \tilde{F}G$ ranges using the 30 FRB samples and our method. The blue points with error bars assume $A_r \tilde{F}G = [0.001, 10] (\text{pc}^2 \text{ km})^{-\frac{1}{2}}$. The orange points with error bars assume $A_r \tilde{F}G = [0.5, 2] (\text{pc}^2 \text{ km})^{-\frac{1}{2}}$. To demonstrate how the result depends on the prior assumption on the $A_r \tilde{F}G$ range, the identical value of $f_{IGM} \times H_0 = 63.2 \text{ km s}^{-1} \text{ Mpc}^{-1}$ is adopted for both cases.

indicating that our method can address the Hubble tension using future FRB samples.

3. We measured a Hubble constant of $H_0 = 74.3^{+7.2}_{-7.5} \text{ km s}^{-1} \text{ Mpc}^{-1}$ with our method using scattering. The central value of this result prefers the measurement from the local distance ladder ($H_0 = 73.0 \pm 1.0 \text{ km s}^{-1} \text{ Mpc}^{-1}$; Riess et al. 2022) over the CMB ($H_0 = 67.7 \pm 0.4 \text{ km s}^{-1} \text{ Mpc}^{-1}$; Planck Collaboration et al. 2020). However, our measurement is still consistent with the two methods within an error of 1σ .

We described two future directions to reduce the error in our measurement. The first direction is to use more localized FRBs with scattering measurements, which are to be detected with future instruments, including BURSTT (Lin et al. 2022). BURSTT is the Taiwanese radio array, which can localize ~ 100 FRBs per year to identify host galaxies with scattering (Lin et al. 2022). The second direction is to statistically treat unlocalized FRBs to further increase the samples (e.g. Zhao et al. 2022).

Acknowledgements. We would like to express our deepest appreciation to the anonymous referee for the comprehensive and thoughtful review of our manuscript. Their detailed examination and insightful suggestions have played a crucial role in refining our work, and the constructive feedback has greatly enhanced the overall quality and clarity of the paper. T-CY is grateful to Ms. Poya Wang for insightful discussions. T-CY is also grateful to Dr. Shotaro Yamasaki for insightful discussions. TG acknowledges the support of the National Science and Technology Council of Taiwan through grants 108-2628-M-007-004-MY3, 111-2112-M-007-021, and 112-2123-M-001-004-. TH acknowledges the support of the National Science and Technology Council of Taiwan through grants 110-2112-M-005-013-MY3, 110-2112-M-007-034-, 113-2112-M-005-009-MY3, and 113-2123-M-001-008-. We acknowledge the use of the CHIME/FRB Public Database, provided at <https://www.chime-frb.ca/> by the CHIME/FRB Collaboration. This research made use of Astropy, a community-developed core Python package for Astronomy (Astropy Collaboration et al. 2018).

References

Astropy Collaboration, Price-Whelan, A. M., Sipőcz, B. M., et al. 2018, AJ, 156, 123

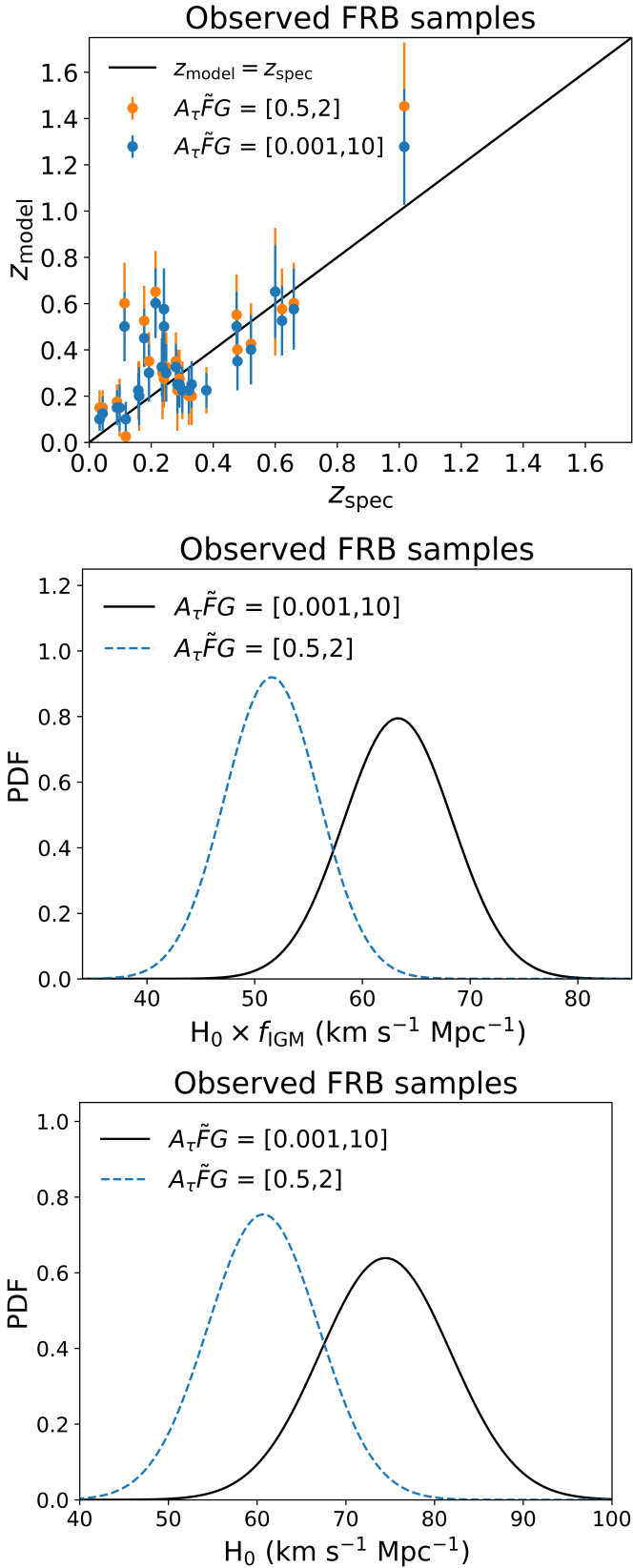


Fig. 13. Comparison between the wide and narrow ranges of AFG. Top panel: Same as Fig. 12, but with optimized $f_{\text{IGM}} \times H_0$ values, where $f_{\text{IGM}} \times H_0$ are $51.5^{+4.4}_{-4.4} \text{ km s}^{-1} \text{Mpc}^{-1}$ and $63.2^{+4.8}_{-5.2} \text{ km s}^{-1} \text{Mpc}^{-1}$ for the narrow and wide $A_T \tilde{F}G$ ranges, respectively. Middle panel: PDF of $f_{\text{IGM}} \times H_0$ using the 30 FRB samples and our method. The solid black line corresponds to the wide $A_T \tilde{F}G$ range, and the dashed blue line corresponds to the narrow $A_T \tilde{F}G$ range. Bottom panel: PDF of H_0 for a given $f_{\text{IGM}} = 0.85 \pm 0.05$ using the 30 FRB samples and our method.

- Bailes, M. 2022, *Science*, 378, abj3043
- Bannister, K. W., Deller, A. T., Phillips, C., et al. 2019, *Science*, 365, 565
- Bhandari, S., Bannister, K. W., Lenc, E., et al. 2020, *ApJ*, 901, L20
- Bhandari, S., Gordon, A. C., Scott, D. R., et al. 2023, *ApJ*, 948, 67
- Bhandari, S., Heintz, K. E., Aggarwal, K., et al. 2022, *AJ*, 163, 69
- Bhandari, S., Kumar, P., Shannon, R. M., & Macquart, J. P. 2019, *The Astronomer's Telegram*, 12940, 1
- Caleb, M., Driessen, L. N., Gordon, A. C., et al. 2023, *MNRAS*, 524, 2064
- Cassanelli, T., Leung, C., Sanghavi, P., et al. 2023, arXiv e-prints, arXiv:2307.09502
- Chawla, P., Andersen, B. C., Bhardwaj, M., et al. 2020, *ApJ*, 896, L41
- CHIME/FRB Collaboration, Amiri, M., Andersen, B. C., et al. 2021, *ApJS*, 257, 59
- CHIME/FRB Collaboration, Andersen, B. C., Bandura, K., et al. 2019, *ApJ*, 885, L24
- Cho, H., Macquart, J.-P., Shannon, R. M., et al. 2020, *ApJ*, 891, L38
- Connor, L., Ravi, V., Catha, M., et al. 2023, *ApJ*, 949, L26
- Cordes, J. M. & Lazio, T. J. W. 2002, arXiv e-prints, astro
- Cordes, J. M., Ocker, S. K., & Chatterjee, S. 2022, *ApJ*, 931, 88
- Day, C. K., Deller, A. T., Shannon, R. M., et al. 2020, *MNRAS*, 497, 3335
- Di Valentino, E., Mena, O., Pan, S., et al. 2021, *Classical and Quantum Gravity*, 38, 153001
- Driessen, L. N., Barr, E. D., Buckley, D. A. H., et al. 2024, *MNRAS*, 527, 3659
- Hagstotz, S., Reischke, R., & Lilow, R. 2022, *MNRAS*, 511, 662
- Hashimoto, T., Goto, T., Chen, B. H., et al. 2022, *MNRAS*, 511, 1961
- Hill, J. C. & Baxter, E. J. 2018, *J. Cosmology Astropart. Phys.*, 2018, 037
- Ho, S. C. C., Hashimoto, T., Goto, T., et al. 2023, *ApJ*, 950, 53
- Hu, J.-P. & Wang, F.-Y. 2023, *Universe*, 9, 94
- James, C. W., Ghosh, E. M., Prochaska, J. X., et al. 2022, *MNRAS*, 516, 4862
- Josephy, A., Chawla, P., Fonseca, E., et al. 2019, *ApJ*, 882, L18
- Kumar, P., Day, C. K., Shannon, R. M., et al. 2020, *The Astronomer's Telegram*, 13694, 1
- Kumar, P., Shannon, R. M., Moss, V., Qiu, H., & Bhandari, S. 2021, *The Astronomer's Telegram*, 14502, 1
- Law, C. J., Butler, B. J., Prochaska, J. X., et al. 2020, *ApJ*, 899, 161
- Law, C. J., Sharma, K., Ravi, V., et al. 2024, *ApJ*, 967, 29
- Lee, K.-G., Khrykin, I. S., Simha, S., et al. 2023, *ApJ*, 954, L7
- Li, Z., Gao, H., Wei, J.-J., et al. 2019, *ApJ*, 876, 146
- Lin, H.-H., Lin, K.-y., Li, C.-T., et al. 2022, *PASP*, 134, 094106
- Lorimer, D. R., Bailes, M., McLaughlin, M. A., Narkevic, D. J., & Crawford, F. 2007, *Science*, 318, 777
- Lorimer, D. R., McLaughlin, M. A., & Bailes, M. 2024, *Ap&SS*, 369, 59
- Macquart, J.-P., Prochaska, J. X., McQuinn, M., et al. 2020, *Nature*, 581, 391
- McQuinn, M. 2014, *ApJ*, 780, L33
- Mena-Parra, J., Leung, C., Cary, S., et al. 2022, *AJ*, 163, 48
- Mörtzell, E., Goobar, A., Johansson, J., & Dhawan, S. 2022, *ApJ*, 935, 58
- Nimmo, K., Hessels, J. W. T., Kirsten, F., et al. 2022, *Nature Astronomy*, 6, 393
- Niu, M., Kasai, A., Tanuma, M., et al. 2022, *Science Advances*, 8, eabi6375
- Petroff, E., Hessels, J. W. T., & Lorimer, D. R. 2019, *A&A Rev.*, 27, 4
- Planck Collaboration, Aghanim, N., Akrami, Y., et al. 2020, *A&A*, 641, A6
- Price, D. C., Foster, G., Geyer, M., et al. 2019, *MNRAS*, 486, 3636
- Prochaska, J. X., Macquart, J.-P., McQuinn, M., et al. 2019, *Science*, 366, 231–234
- Prochaska, J. X. & Neeleman, M. 2018, *MNRAS*, 474, 318
- Prochaska, J. X. & Zheng, Y. 2019, *MNRAS*, 485, 648
- Qiu, H., Shannon, R. M., Farah, W., et al. 2020, *MNRAS*, 497, 1382
- Rafiei-Ravandi, M., Smith, K. M., Li, D., et al. 2021, *ApJ*, 922, 42
- Ravi, V., Catha, M., Chen, G., et al. 2023a, arXiv e-prints, arXiv:2301.01000
- Ravi, V., Catha, M., Chen, G., et al. 2023b, *ApJ*, 949, L3
- Ravi, V., Catha, M., D'Addario, L., et al. 2019, *Nature*, 572, 352
- Ravi, V., Law, C. J., Li, D., et al. 2022, *MNRAS*, 513, 982
- Riess, A. G., Casertano, S., Yuan, W., et al. 2021, *ApJ*, 908, L6
- Riess, A. G., Yuan, W., Macri, L. M., et al. 2022, *ApJ*, 934, L7
- Ryder, S. D., Bannister, K. W., Bhandari, S., et al. 2023, *Science*, 382, 294
- Sammons, M. W., Deller, A. T., Glowacki, M., et al. 2023, *MNRAS*, 525, 5653
- Shannon, R. M. 2023, *Transient Name Server Fast Radio Bursts*, 287, 1
- Shull, J. M. & Danforth, C. W. 2018, *ApJ*, 852, L11
- Simha, S., Lee, K.-G., Prochaska, J. X., et al. 2023, *ApJ*, 954, 71
- Spitler, L. G., Cordes, J. M., Hessels, J. W. T., et al. 2014, *ApJ*, 790, 101
- Tendulkar, S. P., Bassa, C. G., Cordes, J. M., et al. 2017, *ApJ*, 834, L7
- Verde, L., Treu, T., & Riess, A. G. 2019, *Nature Astronomy*, 3, 891
- Wang, Y. & van Leeuwen, J. 2024, *A&A*, 690, A377
- Yamasaki, S. & Totani, T. 2020, *ApJ*, 888, 105
- Zhao, Z.-W., Zhang, J.-G., Li, Y., Zhang, J.-F., & Zhang, X. 2022, arXiv e-prints, arXiv:2212.13433
- Zhou, B., Li, X., Wang, T., Fan, Y.-Z., & Wei, D.-M. 2014, *Phys. Rev. D*, 89, 107303